Contents

Abstract 2

Keywords: 2

1. Introduction 3

2. Simulation Methodology and Device Modeling 5

2.1. Simulation Methodology 5

2.2. Device Modeling 6

3. Results and Discussion 8

3.1. Investigating how the HTL layer's properties are impacted by changes in thickness and doping density on PV solar cell 8

3.2. Examining the effects of varying thickness and doping density on the $MoTe_2$ absorber layer 10

3.3. The role of $MoTe_2$ thickness and defect density in shaping the properties of PV Structure 11

3.4. Analysing the effects of altering the temperature and rare surface recombination velocity on PV Structure 13

3.5. Exploring how the PV parameters of the solar cell are affected by its interface defect density 14

3.6. Understanding the effects of series and shunt resistance on the PV performances 16

3.7. The CV characteristics of the optimized device 17

3.8. The final output performance $MoTe_2$ solar structure 20

4. Conclusions 22

Disclosures: 23

Acknowledgement: 23

References 23

Enhancing Efficiency in MoTe2-Based Solar Cells: The Impact of Sb2S3 Hole Transport Layer and Thickness Optimization

Md. Arifur Rahman[1], Md. Dulal Haque[2], Md. Hasan Ali[3] and Abu Zafor Md. Touhidul Islam[1,*]

[1]Department of Electrical and Electronic Engineering, University of Rajshahi, Rajshahi-6205, Bangladesh

[2]Department of Electronics and Communication Engineering, Hajee Mohammad Danesh Science and Technology University, Dinajpur-5200, Bangladesh

[3]Department of Electrical and Electronic Engineering, Begum Rokeya University, Rangpur; Rangpur-5400, Bangladesh

*Corresponding author: touhid.eee@ru.ac.bd

Abstract

In this study, SCAPS-1D simulator was used to investigate the performance of a solar cell structure based on Molybdenum Telluride ($MoTe_2$) with Sb_2S_3 (Antimony Sulfide) Hole Transport Layer (HTL). The motivation behind choosing $MoTe_2$ as an absorber layer for its higher optical absorption efficiency, cost-effectiveness, reliable and stable operation. The comparative study of this introduced (Al/FTO/CdS/$MoTe_2$/Sb_2S_3/Pt) and baseline solar cell (Al/FTO/CdS/$MoTe_2$/Pt) has been implemented. Various photovoltaic parameters like open-circuit voltage, short-circuit current, fill factor, and efficiency have been investigated varying absorber and HTL thickness, doping density, rare surface recombination velocity, defect density, series as well as shunt resistance and temperature. The proposed solar cell performance of η, $V_{oc,}$ $J_{sc,}$ and FF was found to be 40.33%, 1.13 V, 40.78 mA/cm^2, 87.63% optimizing absorber thickness value of 0.5 μm and doping concentration value of 5×10^{16} cm^{-3}. The determined values of performance parameters V_{oc}, $J_{sc,}$ FF, and η are 0.95 V, 38.15 mA/cm^2, 81.09% and 29.35%, respectively for baseline solar cell. The implantation of Sb_2S_3 layer contributes to improve the performances by diminishing carrier recombination losses. The present research results indicate the feasible way for obtaining a lower-cost, and higher-efficiency $MoTe_2$-based SC with Sb_2S_3 HTL layer.

Keywords: TMDC, $MoTe_2$, Sb_2S_3 HTL, Solar cell, SCAPS 1D, and Efficiency.

1. Introduction

The demand for energy is constantly growing up all across the world. The availability of suitable energy sources is diminishing regularly since there are no available specialized energy storage systems. As a result, a clean energy source that is renewable, long-term, cost-effective, and environment-friendly is required, and solar energy is a candidate here. Solar cells are an excellent choice since they reduce the power generation cost and minimize the need for fossil fuels [1] [2]. Photovoltaic solar cells made of polycrystalline silicon lead the worldwide market and contribute to over 90% of total PV manufacturing [3] [4]. The drawbacks of Si solar structure are massive production charge and low efficiency. The highest power conversion efficiency was recorded at 26.7 % and 24.4 % for crystalline and polycrystalline Si-based PV cells [5]. Nowadays, researchers have been concentrating their attention on manufacturing highly effective thin-film solar cells (TFSCs) using earth-abundant, non-poisonous, and suitable materials. Among the TFSCs materials, Molybdenum Ditelluride ($MoTe_2$) is a very much effective and promising absorber materials because of its non-poisonous, stability, and cost-effectiveness. It is a transitional dichalcogenide materials (TMDs) with layered architecture of MX_2, where M = (Mo, W) is the infusion atom belonging to groups 3 to 12 and X = (S, Se, Te) is the chalcogen atom belonging to group 16. The various electronic, optical, catalytic, and magnetic characteristics of TMDs materials have been intensively studied by several research groups [6] [7] [8]. $MoTe_2$ has a sandwiched structure similar to conventional TMDs, and the weak Van Dar Waals forces bind the atoms together [6] [7]. The textured crystalline of $MoTe_2$ with the orientation of the c-axis perpendicular to the plane of the grains may contribute to perform as an effective absorber layer [9]. $MoTe_2$ is a TFSCs material having high carrier flexibility and lower defect density [7] [8]. The advantages of MoTe2 thin films are optical absorption higher than 10^5 cm^{-1}, efficient, cost-effective fabrication process, reliable and stable operation as well as long-term stability. The direct bandgap of $MoTe_2$ is 1.1 eV with an intense work function value of ~4.7 eV which enables an expansion of optoelectronic applications from the visible to the infrared spectrum [9] [10] [11]. While, most of the TMDC materials such as $MoSe_2$, WS_2 and MoS_2 operate in the visible range [12]. Experimental and theoretical research on TFSCs by utilizing the $MoTe_2$ absorber layer has been reported by several research groups.

The η, FF, $V_{oc,}$ J_{sc} of the $SnO_2/Zn_2SnO_4/CdS/MoTe_2/Mo$ Solar structure had been recorded to be 17.06 %, 73%, 0.730 V and 23.74 mA/cm^2 respectively. By inserting an As_2Te_3 HTL layer within the left metal contact and absorber in this same structure, the performances of η, FF, V_{oc} and J_{sc} enhanced to 25.06 %, 84.7%, 1.8 V, and 27.60 mA/cm^2, respectively [10]. The same research groups investigated the structure $SnO_2/Zn_2SnO_4/CdS/MoTe_2/Mo$ with different BSF layers to increase the behaviour of this solar cell. The η determined was 25.11 %, 25.16 %, and 25.17% for CZT, ZnTe, and In_2Te_3 HTL, respectively [13] [11] [14]. The conversion efficiency of approximately 15.45% had been observed for FTO/CdS/$MoTe_2$/Ag solar cell and the highest PCE of 29.13% had been attained for optimized FTO/ZnO/$MoTe_2$/Cu_2Te_3/Ni cell at 1500 nm thickness [1]. But higher efficiency can achieve from the bilayer structure such as for bilayer Graphene/HgCdTe dual and single junction photodetector efficiency is 85.8 and for bilayer, Graphane/ZnO/Silicon heterojunction efficiency is 71% [15].

Since the determined behaviour of the parameters of this introduced $MoTe_2$ solar cell cannot compete with other heterojunction TFSCs. The conventional $MoTe_2$ solar cells are needed to be remodelled to achieve excellent performance after inserting a useful hole transport layer within the absorber and the left metal electrode. Band alignment and band gap tuning between the HTL and absorber layer are also crucial. Therefore, it's important to continue more research work for achieving better performance of the $MoTe_2$ absorber layer. Herein, both V_{oc} and J_{sc} are the essential criteria for enhancing the η of $MoTe_2$ SC. The obtained values of V_{oc} and J_{sc} of the $MoTe_2$ solar are still lower than the expected results because of the recombination of the carrier at the intersection. Besides, the inefficient carrier transportation and collection in the electrodes instead of the recombination of the carrier in the interface causes the reduction of the V_{oc} and J_{sc} which results in lower photo conversion efficiency [16][17]. Therefore, redesigning the $MoTe_2$ solar cell with useful HTL is also essential.

An HTL layer with commendable bodily properties, optical behaviour, and chemical stability may simplify the exact transportation and collection of photo-generated carriers between the absorber and metal electrode. The HTL layers of $NiO_{2,}$ CuI, Sb_2S_3, CuSCN or CuO_x have been employed in various types of solar cells [18][19][20][21]. Among them, Sb_2S_3 is a very much useful and cost-effective material which can be used as an HTL layer. The Sb_2S_3 is suitable as a transportation layer with a larger band gap, earth-abundant, non-poisonous, and useful for band matching. A

suitable band alignment is anticipated by introducing Sb_2S_3 between the absorber and the left contact which will be benefited for the transportation of the hole and restrict electrons from the absorber layer [22]. Therefore, the photo-generated carriers (holes) can able to transport to the left metal contact through Sb_2S_3 and minority carrier electrons are inhibited by the potential barrier which was developed at $Sb_2S_3/MoTe_2$ interface.

2. Simulation Methodology and Device Modeling

2.1. Simulation Methodology

So many tools are used by the researchers for analysis of the characteristics of the TMSCs like COMSOL, SILVACO ATLAS, AMPS, SCAPS etc. [23]. In this study, we conducted our research using SCAPS software (Version 3.3.05) which is a one-dimensional simulator (SCAPS-1D) software. It has been employed for modelling and simulation works that were developed at Electronics & Information System (EIS) department at Gent University, Belgium. The exploration of the different physical parameters has been done by utilizing carrier transport equations [24]. This simulation software has also been applied for elementary semiconductor equations like electrons and holes transportation, Continuity, and Poisson equations. It may extract the J_{sc} vs V_{oc} (J-V) curve and also the ac characteristic curves like C-F, C-V, and η curve of a PV SC. The performances of this presented structure have been analyzed to exhibit the outcomes of defect density, doping concentration, thickness, temperature, rare contact work function, R_s and R_{sh} using the SCAPS-1D program. The simulations were carried out below the enlightenment of AM1.5G at a working temperature of 300 K.

The SCAPS analysis is based on Poisson's equation, electron continuity and hole continuity, mentioned below [24]:

$$\frac{\partial^2 \Psi}{\partial x^2} + \frac{q}{\varepsilon}[p(x) - n(x) + N_D - N_A + \rho_p - \rho_n] = 0 \quad \ldots\ldots\ldots\ldots\ldots\ldots\ldots\ldots (1)$$

$$\frac{1}{q}\frac{dJn}{dx} = -G_{op}(x) + R(x) \quad \ldots\ldots\ldots\ldots\ldots\ldots\ldots\ldots\ldots\ldots\ldots\ldots (2)$$

$\frac{1}{q}\frac{dJp}{dx}$= $G_{op}(x)$-R(x) … … … … … … … … … … … … … … … … (3)

Where, Ψ, $N_{D,}$ $N_{A,}$ ρ_p, $\rho_{n,}$ q, $Jp, Jn,$ are the electrostatic potential, donor density, acceptor density, hole distribution, electron distribution, electron charge, current densities of hole and current densities of electrons respectively stated as a function of the position coordinate x.

2.2. Device Modeling

Figures 1(a)-(b) display the structural design of the proposed Al/FTO/CdS/$MoTe_2$/Sb_2S_3/Pt SC and the energy band diagram, respectively. In this model, a p-type $MoTe_2$ has chosen as the absorber layer and CdS is the n-type buffer layer. The p^+-type Sb_2S_3 HTL layer is implanted in between the absorber and rare contact layer. The FTO has been devoted to a layer of translucent directing oxide (TCO).

The Pt and Al have been used as the rare and right contact respectively. The values of the physical parameters of several layers have been listed in Table 1. We carefully accumulated these values from several experimental and theoretical works. Table 2 includes the values of the interface defect parameters. The hole and electron thermal velocity are considered 10^7cm/s at room temperature. The absorption coefficient values of Sb_2S_3, $MoTe_2$, CdS, and FTO has received from the SCAPS-1D program model [25]. The exterior recombination rate of electrons and holes has assumed 10^7cm/s for both the back and front sides. For the simulation, the capture cross-section of both hole and electron has been chosen as 10^{-19} cm^{-2}.

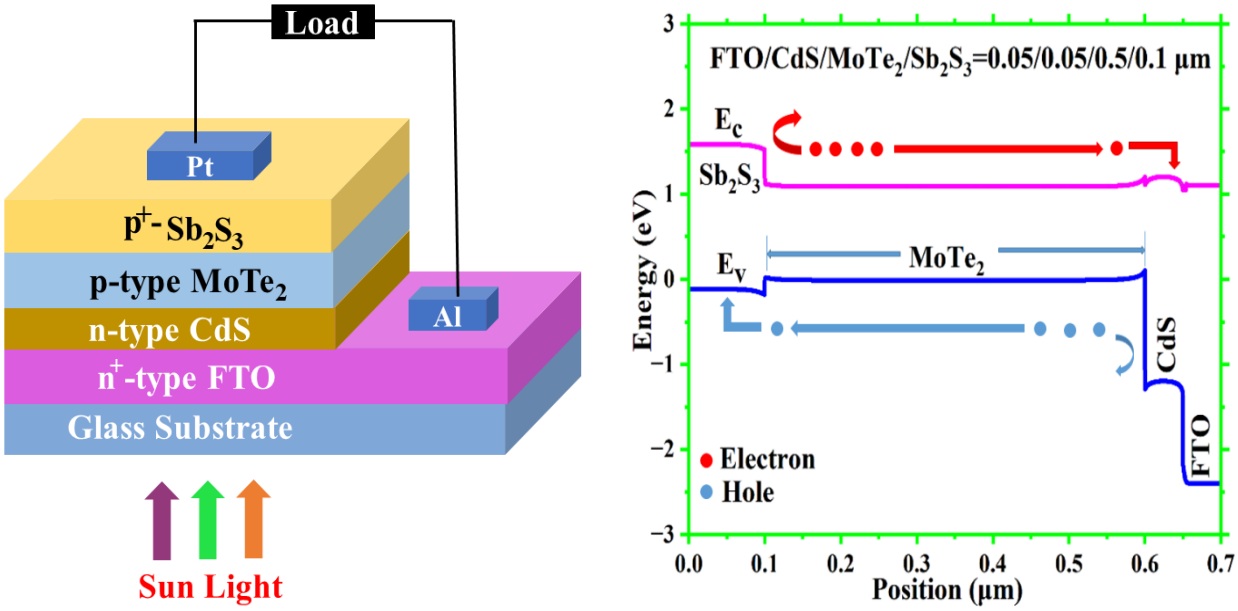

(a) (b)

Fig: 1. (a) The structural design and (b) illuminated energy alignment of the Al/FTO/CdS/$MoTe_2$/Sb_2S_3/Pt Solar Structure.

Table 1: Physical input parameters utilized of $MoTe_2$-based structure required in the simulation [11] [22].

Parameters (unit)	FTO	CdS	$MoTe_2$	Sb_2S_3
Thickness (nm)	50	50	100 - 1500	10 - 120
Band Gap, E_g(eV)	3.5	2.4	1.1	1.7
Electron Affinity, χ (eV)	4	4.3	4.2	3.8
Dielectric Permittivity, ε_r	9	10	13	7
CB effective density, N_c (cm^{-3})	2.2×10^{18}	1.8×10^{7}	10^{7}	10^{19}
VB effective density, N_v (cm^{-3})	10^{19}	10^{17}	2.4×10^{19}	1.8×10^{19}
Electron Mobility, μ_e (cm^2/V-s)	20	350	110	0.07
Hole Mobility, μ_h(cm^2/V-s)	10	25	426	0.02
Donor Density, N_D(cm^{-3})	10^{19}	10^{17}	0	0
Acceptor Density, N_A(cm^{-3})	0	0	5×10^{13}- 5×10^{22}	$10^{11}-10^{22}$
Defect Type		SA		SD
Defect Density, N_t (cm^{-3})	10^{14}	10^{14}	$10^{12} - 10^{21}$	10^{14}
Energetic Distribution		Gaussian	Gaussian	Gaussian

Table 2: Boundary constraints cast-off in Al/FTO/CdS/$MoTe_2$/Sb_2S_3/Pt heterojunction cell.

Parameters (unit)	$MoTe_2$/Sb_2S_3 interface	CdS/$MoTe_2$ interface
Category of Defect	Neutral	Neutral
Capture cross-section of electrons (cm^{-2})	10^{-19}	10^{-19}
Capture cross-section of holes (cm^{-2})	10^{-19}	10^{-19}
Position for imperfection energy level, E_t	Above the highest E_v	Above the highest E_v
Energy regarding reference (eV)	0.6	0.6
Total density (cm^{-2})	$10^{10} - 10^{20}$	$10^{10} - 10^{20}$

3. Results and Discussion

3.1. Investigating how the HTL layer's properties are impacted by changes in thickness and doping density on PV solar cell

The proper transportation and collection of photo-generated holes can be obtained by the suitable HTL layer and it can also restrict the flow of electrons (minority carrier). As a result, it reduces carrier recombination. Hence, it's highly essential to demonstrate the consequences of the HTL layer on SC performance parameters. The effect of thickness and doping density of Sb_2S_3 on the performance parameters of the proposed SC has been represented in Fig. 2. The values of thickness have been changed within 10 to 120 nm and the value of doping concentration within 10^{11} to 10^{22} cm^{-3}, respectively, while other parameters remain constant. The values of V_{oc} and J_{sc} act with a little variation with rising the thickness of the HTL layer. However, the FF and η demonstrate an almost insignificant amount of reduction. The parameter values of V_{oc}, FF, and η initially show a constant tendency with increasing the doping concentration of the HTL layer upto 10^{21} cm^{-3}. After that, it rises slightly when the doping density is more than 10^{21} cm^{-3} and maintains a constant value. The increase in doping concentration may contribute to reduce the recombination of carriers that facilitate proper transportation and collection of carriers and as a result the rise in the performances of V_{oc}, FF, and η. The decrease of FF with reducing doping concentration in Sb_2S_3 HTL indicates

the rise of series resistance in the introduced solar cell [26][27]. The optimal thickness may be considered as 100 nm and the optimal doping density may be considered to be and 10^{18} cm^{-3} for obtaining the maximum η of 40.33%.

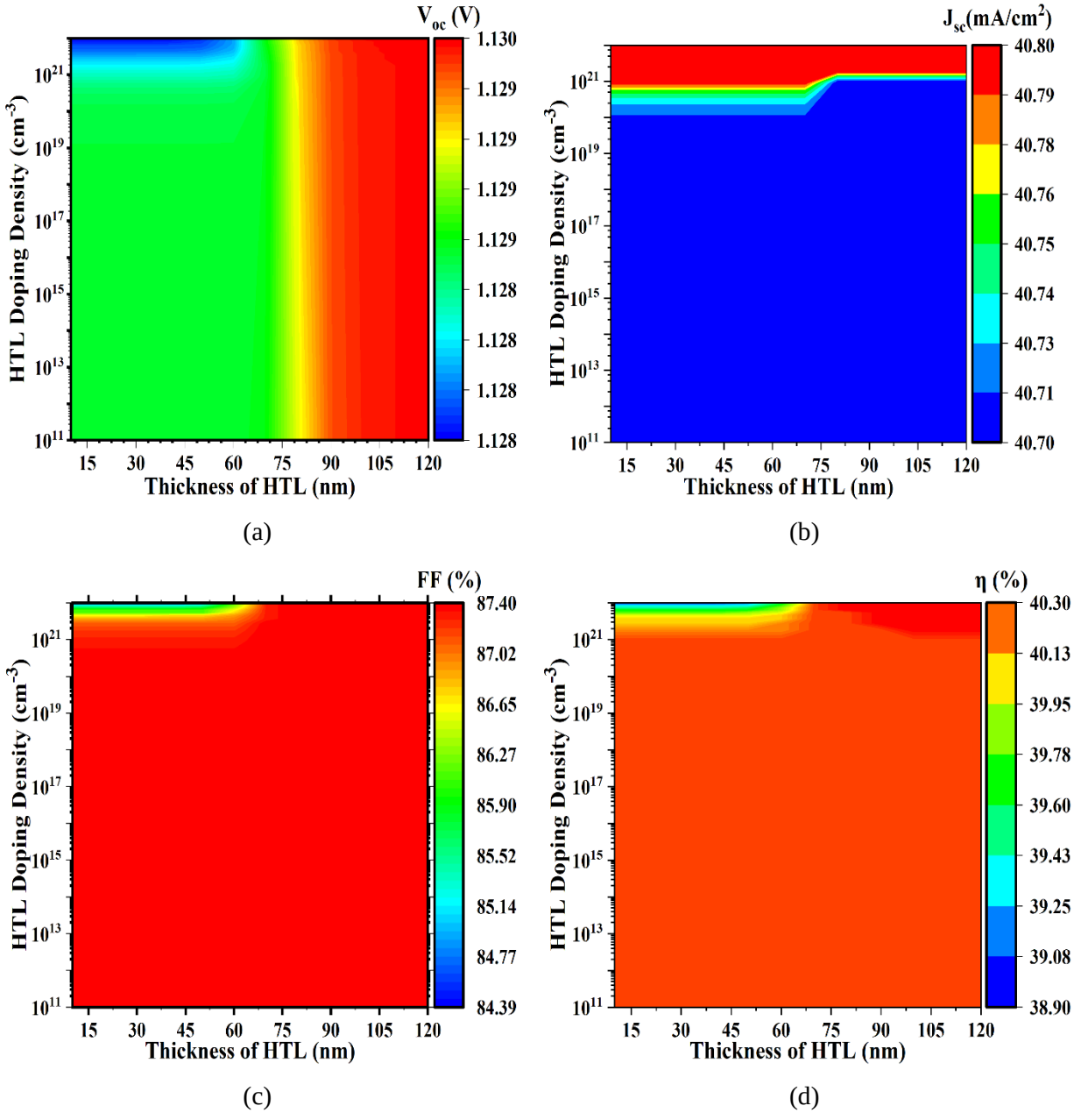

Figure 2. HTL thickness and doping density has varied for presenting the parameters of (a) V_{oc} (b) J_{sc} (c) FF and (d) η.

3.2. Examining the effects of varying thickness and doping density on the $MoTe_2$ absorber layer

The simultaneous influence of the $MoTe_2$ layer on the performances with the variation of thickness and carrier concentration has been observed and narrated in Fig. 3. The percentage of incident photons entered into the $MoTe_2$ contributes for enhancing J_{sc} and V_{oc} changes because of absorber concentration. Thus, it's highly needed to optimize the thickness as well as carrier density. These values have been switched within 100 to 1500 nm and 10^{13} to 10^{22} cm^{-3}, respectively. It has been demonstrated that V_{oc} enhances due to the rise of the doping concentration while J_{sc} reduces. On the contrary, the increase in thickness reduces V_{oc} below the doping concentration of 5×10^{17} cm^{-3} and then it rises marginally. The FF and η rise because of the enhancement of the two varied parameters (thickness and doping concentration). The higher thickness of the $MoTe_2$ contributes to enhance the absorption of the incident photons which displays higher values of η, FF and Jsc. The rise of doping density may also attribute to enhance the carrier recombination rate and hence, the value of J_{sc} and V_{oc} reduces [28] [29] [30]. At a thickness value of 500 nm and doping concentration of 5×10^{16} cm^{-3}, the numerically simulated value of η, FF, V_{oc}, and J_{sc}, is 1.13 V, 40.78 mA/cm^{-2}, 87.63%, and 40.33%, respectively. For achieving a better performance of Al/FTO/CdS/$MoTe_2$/Sb_2S_3/Pt SC, we consider the optimum points of doping density and thickness to be 5×10^{16} cm^{-3} and 500 nm, respectively

.

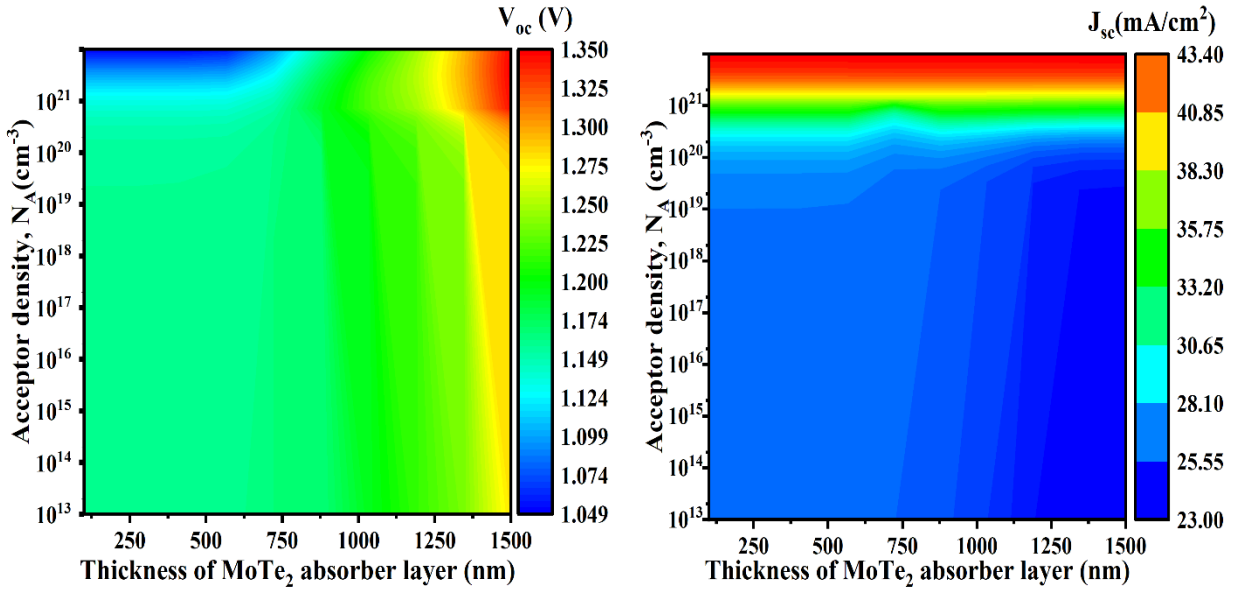

(a) (b)

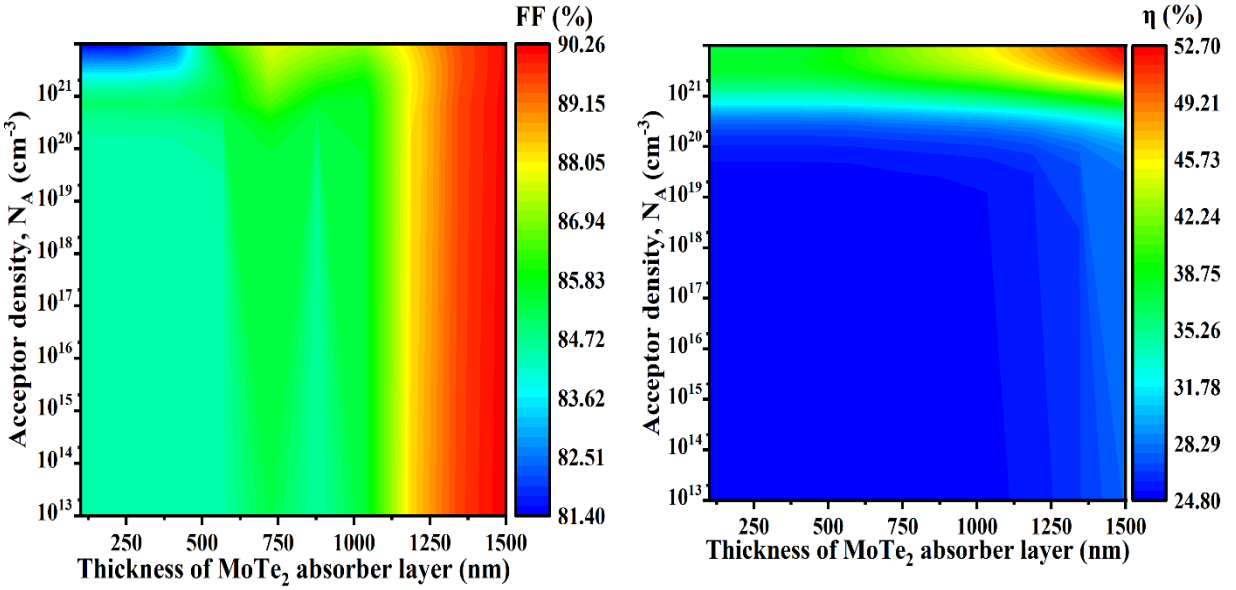

(c) (d)

Figure 3. Absorber ($MoTe_2$) thickness and doping density has varied for presenting the parameters of (a) V_{oc} (b) J_{sc} (c) FF and (d) η.

3.3. The role of $MoTe_2$ thickness and defect density in shaping the properties of PV Structure

The presence of defects in the SC system has an opposing impact on PV performances. For that, it's highly beneficial to supervise the impact of defect density on the $MoTe_2$ layer. The simultaneous influence of defect density and thickness of $MoTe_2$ on device performances FF and has defined in Fig. 4. It is noticeable that the parameters values of V_{oc}, J_{sc}, FF and η have been decreased from 1.24 to 1.00 V, 40.77 to 17.32 mA/cm^{-2}, 83.19 to 44.18%, and 42.05 to 5.62% respectively for changing the defect density within 1.0×10^{12} to 1.0×10^{21} cm^{-3} at a constant thickness of 500 nm. The PV parameters enhance with the rising thickness up to the defect density 10^{18} cm^{-3} and reduce after that limit. Whereas values of V_{oc} reduce noticeably with rising thickness. The simulated results demonstrate a clear correlation between defect density and the reduction in parameter values for the $MoTe_2$ SC. Shockley Red Hall recombination losses are influenced by defects located within the band gap of the absorber layer. A consequence of the SRH mechanism is the reduction in photo-generated carriers, leading to diminished SC performances [31] [32] [33]. At the defect density of 10^{14} cm^{-3} and thickness of 500 nm, the numerically simulated determined performance parameters of V_{oc}, J_{sc}, FF and η are 1.33 V, 40.78 mA/cm^{-2}, 87.68% and 40.33%, respectively. We have chosen the value of defect density and thickness 10^{14} cm^{-2} and 500 nm, respectively for determining the optimum performance of the displayed solar cell. By setting the

defect density at 10^{14} cm^{-2} and thickness at 500 nm, we aimed to determine the best performance for the SC presented.

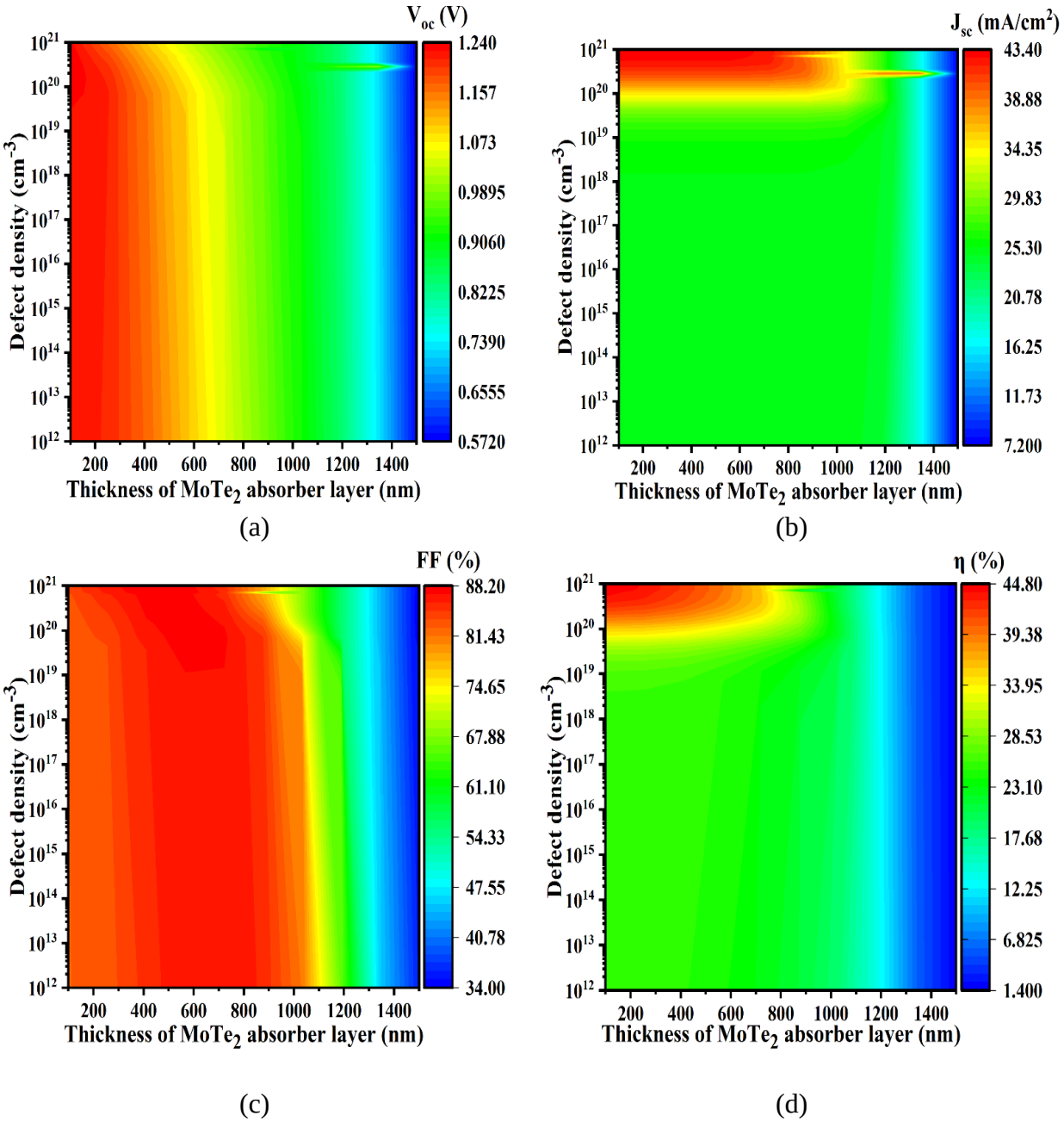

Figure 4. Absorber ($MoTe_2$) thickness and defect density has varied for displaying the parameters of (a) V_{oc} (b) J_{sc} (c) FF and (d) η.

3.4. Analysing the effects of altering the temperature and rare surface recombination velocity on PV Structure

The simulation work, displayed in Fig. 5(a), investigated the influence of working temperature (ranging from 274 K to 525 K) on the performance of the $MoTe_2$ SC. Increasing the working temperature shows a consistent reduction in the PV performances except for $J_{sc.}$ It has been noticed that the value of all the PV parameters (V_{oc}, FF, and η) decreases monotonically except J_{sc} with increasing the operating temperature. The numerically simulated η for the SC without the HTL layer is 29.63% and 22.28% at a temperature of 275K and 525K, respectively. While the maximum η of the newly designed SC with Sb_2S_3 HTL is 40.76% and 32.97% at the temperature of 275K and 525K, respectively. Increased working temperature promotes greater collision rates between photogenerated electron-hole pairs and vibrational atoms, resulting in J_{sc} fluctuations in the proposed SC. The diminishing energy bandgap in the semiconductors, caused by the increasing temperature, is responsible for the drop in V_{oc} [34] [35]. These outcomes are consistent with the findings of multiple research groups investigating temperature-related effects on PV performances [35,36].

. The examination of the back surface recombination velocity (BSRV) on the PV performances has been carried out for the SC, with and without HTL and is visually represented in Fig. 5(b). It can demonstrate a reduction in the values of V_{oc}, J_{sc}, FF, and η has been reduced from 1.13 to 0.91V, 40.70 to 36.00 mA/cm^{-2}, 87.4 to 77.8% and 40.33 to 25.20%, respectively for changing BSRV from 1×10^{1} to 1×10^{5} cm/s for the baseline Solar structure. No significant changes are observed in the PV performances as BSRV varies, indicating consistent behaviour. The insertion of the HTL layer creates a high electric field which contributes to decreasing the recombination loss. Therefore, the PV parameters remain constant. On the contrary, the absence of HTL accelerates the recombination and the PV parameters reduce [37] [38].

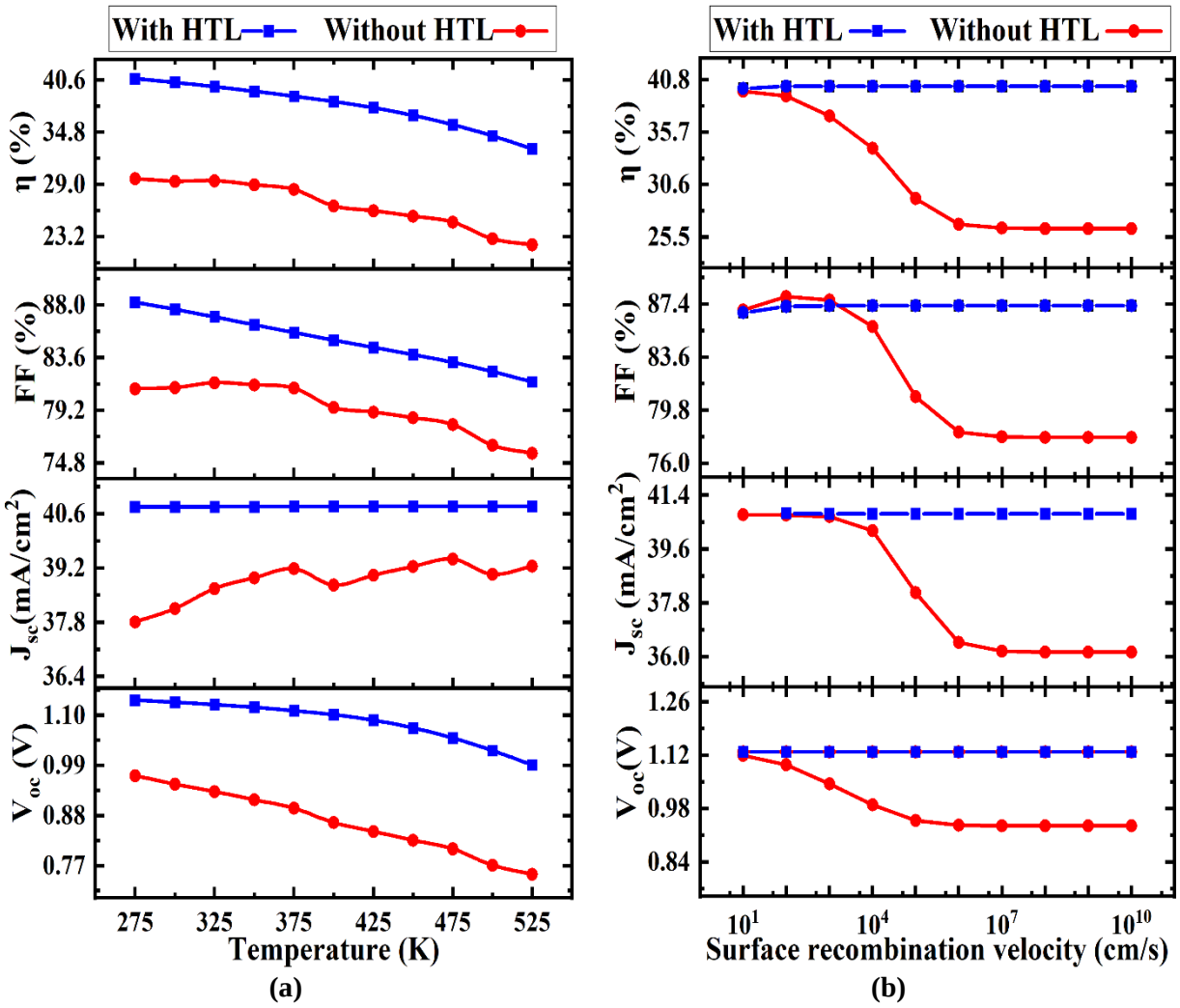

Figure 5. Variation of Photovoltaic parameters of $MoTe_2$ SC with (a) temperature and (b) BSRV.

3.5. Exploring how the PV parameters of the solar cell are affected by its interface defect density

We have investigated the effect of defect density at $MoTe_2/Sb_2S_3$ and $MoTe_2$/CdS interfaces of the $MoTe_2$ heterojunction SC under the enlightenment of AM1.5G and 300 K temperature as represented in Fig. 6 (a) and (b). The variation of defect density within 10^{10} to 10^{20} cm^{-2} is applied at the interface of $MoTe_2/Sb_2S_3$ keeping others parameters fixed. The results demonstrate a constant behaviour in all PV parameters up to 10^{14} cm^{-2}, followed by a decrease in response to rising defect density.

At the CdS/$MoTe_2$ interface, higher defect density results in a significant drop in the values of FF, η and V_{oc}. The values of Jsc remains unaltered at 40.87 mA/cm^2 until the defect density reaches 10^{16} cm^{-2}. The degradation of η and V_{oc} from 40.33 to 27.30% and 1.1 to 0.3 V for altering the defect density in between 10^{10} cm^{-2} to 10^{20} cm^{-2}, respectively. The defect density at CdS/$MoTe_2$ interface has a dominant impact over that of the $MoTe_2/Sb_2S_3$ interface of the demonstrated structure. The interface defects contribute to increasing the rate of photo-generated carrier recombination which degrades the PV performances [29] [39] [40]. The optimum performance was achieved at the position of 10^{14} cm^{-2} of the defect density for both interfaces. The trap state exists at the interfaces behave like a recombination centre and contributes to the degradation of the photo-generated carriers. In this way, the interface defects demand a reduction in the performance of the SC [41].

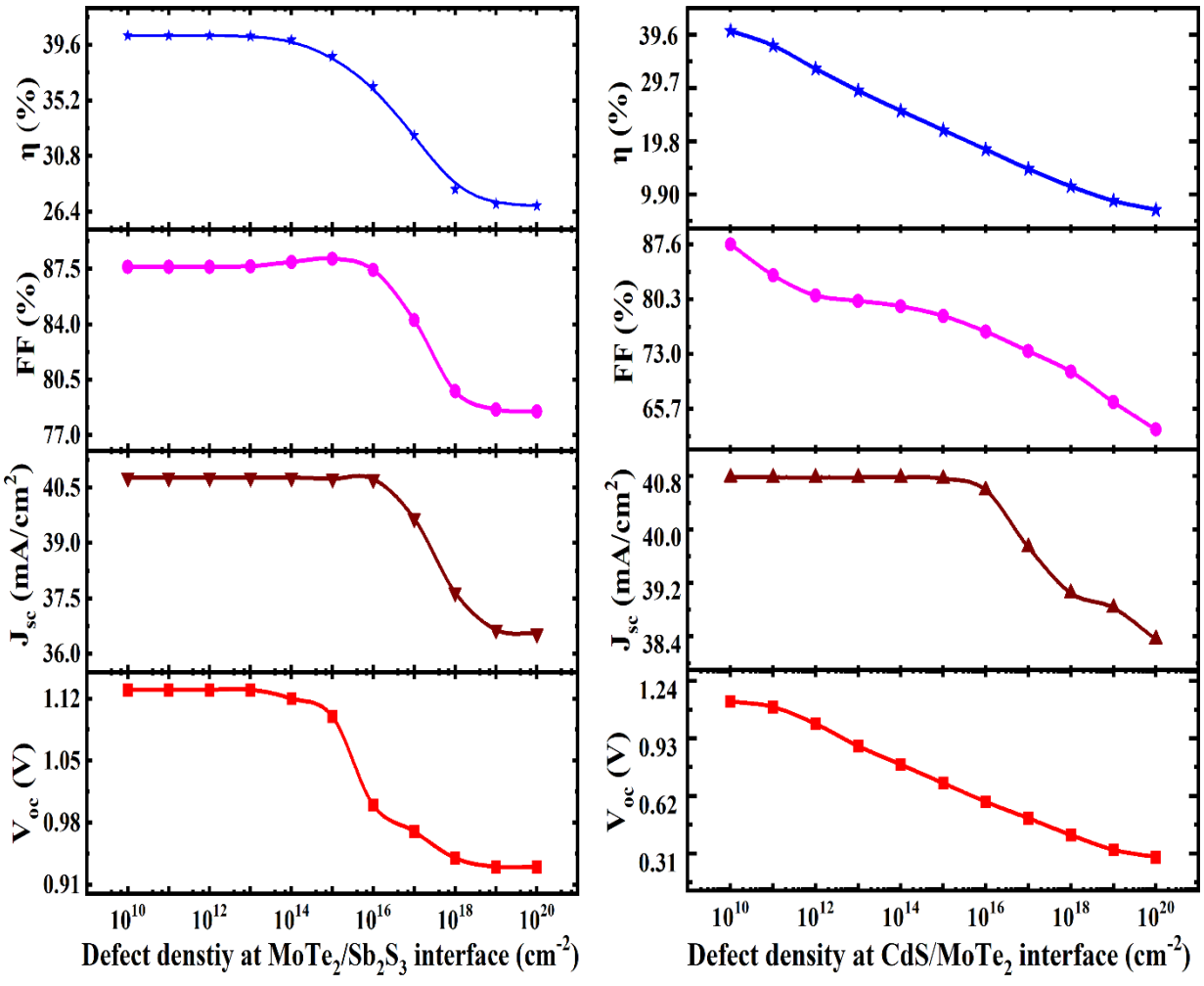

(a) **(b)**

Figure 6. Influence of interface defect at (a) $MoTe_2/Sb_2S_3$ and (b) $CdS/MoTe_2$ interfaces on the PV parameters.

3.6. Understanding the effects of series and shunt resistance on the PV performances

Several factors are liable for the non-ideality behaviour of a solar structure. One of them is parasitic resistance (R_s & R_{sh}). Both these resistances diminish the output performances of the solar structure. The R_s and R_{sh} resistance significantly affects SC performance parameters. The R_s originated from the connection among various terminals between front and back contact in the heterojunction SC structure. In contrast, R_{sh} is generated from defects in the SC that cause to increase in reverse saturation current. Therefore, these resistances have a significant role in SC PV performance.

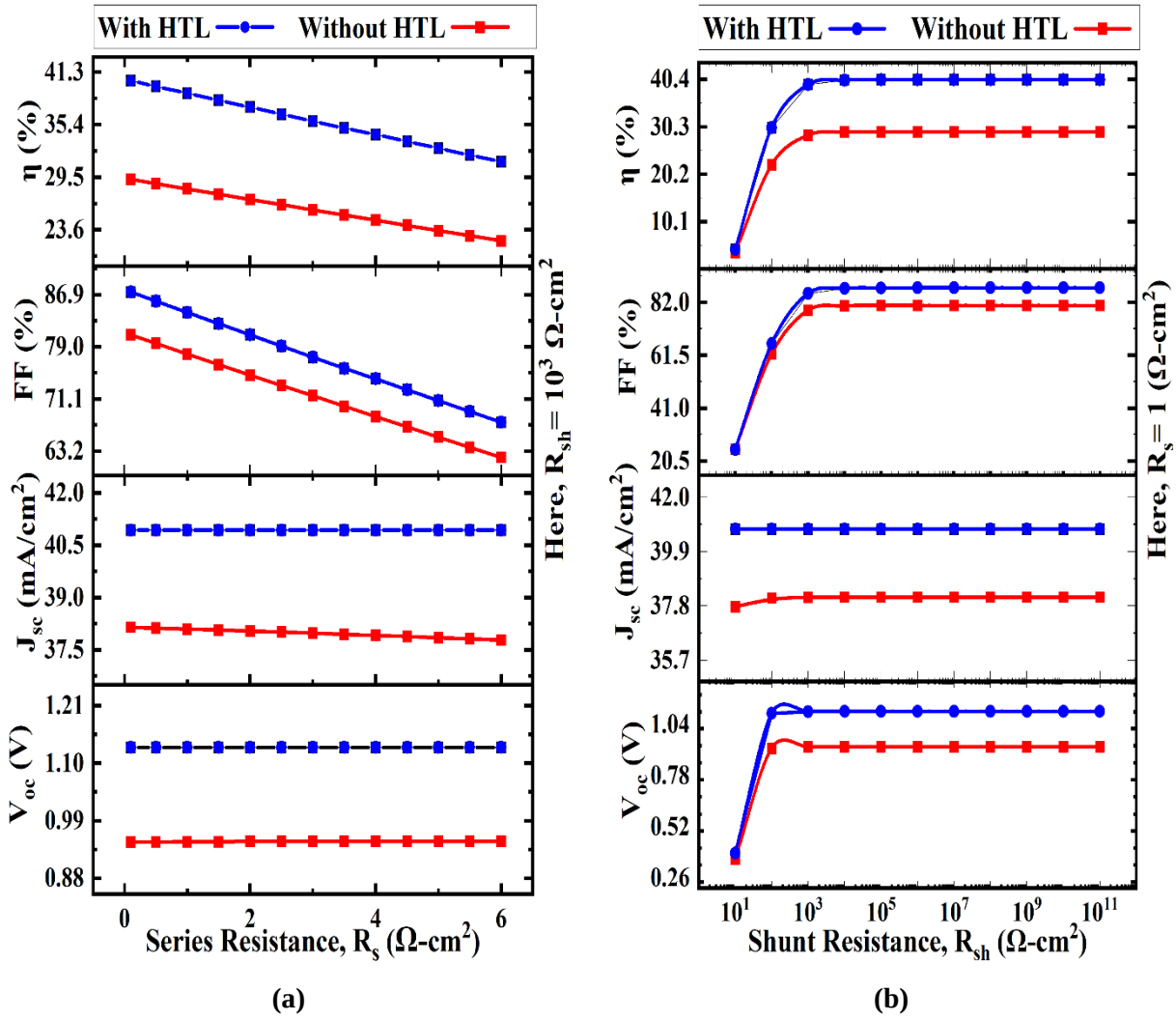

Figure 7. Comprehensive analysis of (a) series and (b) shunt resistances to enhance the overall performance of $MoTe_2$ SC.

Fig. 7 (a) and (b) present a comparative analysis of how R_s and R_{sh} affect the PV parameters of the $MoTe_2$ structure, both in the absence and presence of an Sb_2S_3 HTL. The values of FF, and η reduces with the variation of R_s from 0 to 6 Ω-cm^2 at a fixed R_{sh} of 10^3 Ω-cm^2. Otherwise, values of V_{oc} and J_{sc} remain fixed over the entire range of R_s. The improper connection at the front contact, back contact and combination among various terminals causes power loss which in turn outcomes in a fall down in the conversion efficiency [28][42]. With the enhancement of R_s, the behaviour of FF decreases dramatically because of solder bond degradation, but the Jsc drop for the optical transmission loss resulted from the encapsulate discolouration [43].

Furthermore, we have investigated the effect of R_{sh} on PV parameters by altering values within 10^1 to 10^{11} Ω-cm^2 at constant R_s of 1 Ω-cm^2 and displayed in Fig. 7(b). From the simulated results, it is highly noticeable that the performance parameters enhance with increasing the R_{sh} except J_{sc} which is constant. The parameters values increased up to 10^3 Ω-cm^2, and then got saturated above the 10^3 Ω-cm^2. The calculated η has been determined 4.16% and 40.33% at the R_{sh} value of 10^3 to 10^6 Ω-cm^2, respectively. The presences of bulk and interface defects in the proposed Al/FTO/CdS/$MoTe_2$/Sb_2S_3/Pt SC are liable for decreases in the values of R_{sh} which in turn reduces the PV performance parameters [28] [44].

3.7. The CV characteristics of the optimized device

To characterize the semiconductor devices like solar cells, the C-V profile is an integral part and is used to enhance the device's performance. This study reveals additional basic features of a device structure, where doping density and build-in potential can be derived with the help of two following relations [24]:

$$\frac{1}{C^2}=\frac{2}{qN_a\varepsilon_0\varepsilon_s A^2}(V_{bi}-V) \quad \ldots\ldots\ldots\ldots\ldots\ldots\ldots\ldots\ldots\ldots \quad (4)$$

$$N_a=\frac{2}{q\varepsilon_0\varepsilon_s A^2\left[\frac{d}{dv}\left(\frac{1}{c^2}\right)\right]} \quad \ldots\ldots\ldots\ldots\ldots\ldots\ldots\ldots\ldots\ldots\ldots \quad (5)$$

Where, the mentioned C, N_a, ε_0, ε_s, A, V, q are the values of measured capacitance, doping density (1/cm^3), the permittivity of the free space (8.85×10^{-14} F/cm, dielectric constant as per table 1, area

of the cell (cm^2), applied potential, the charge of an electron (1.6×10^{-19} C), respectively. From these two relations, we can find the build-in potential (V_{bi}) and doping density (N_a) from the intercept and the slope of the line in C^{-2} vs V plot.

To evaluate the consistency of the studies, the C-V measurements may examine at diverse frequencies ranging from 0.1 kHz to 1 MHz. The total p-n junction may be the summation of the diffusion and depletion capacitance. At forward bias, the depletion capacitance is smaller than diffusion capacitance, while the relationship is opposite for reverse biased condition. At zero bias condition, the capacitance is found 48 nF/cm^2 as shown in Figure 10 (a). The mathematical expression for the depletion capacitance is as follows [45]:

$$C(V)=A\sqrt{\frac{Nq\varepsilon_0\varepsilon_s}{2(V_{bi}-V)}} \quad \ldots\ldots\ldots\ldots\ldots\ldots\ldots\ldots\ldots\ldots\ldots\ldots\ldots\ldots\ldots\ldots (6)$$

Their physical meanings are stated above. At a constant frequency, the capacitance exhibits a substantial and rapid rise with the increasing polarization potential. The Mott-Schottky plot of the proposed structure is shown in Figure 10 (b). The intersection of the $1/C^2$ with the voltage axis originates the flat band potential. Here, the negative slope reveals that holes are the majority carrier and electrons are the minority carrier and the space charge area broadly occupies the p-type $MoTe_2$ absorber layer. Localized deep states in the $MoTe_2$ layer lead to a noticeable marginal deviation in the $1/C^2$ curve. The C-V characteristics with varying absorber layer thickness (0.1 μm to 0.8 μm) are shown in Fig. 10 (c), keeping frequency constant at 1 MHz. The capacitance value is almost constant up to a certain level and changes dramatically after that level. The same kind of relation has been discussed in the earlier report [46].

The C-V characteristics with varying absorber doping density at a constant frequency of 1 MHz has studied in Fig. 10 (d). With the increases in bias voltage, the capacitance value also changes proportionally. The charge development at the interface increases with the increases in absorber doping density which further contributes to enhancing the capacitance value [41].

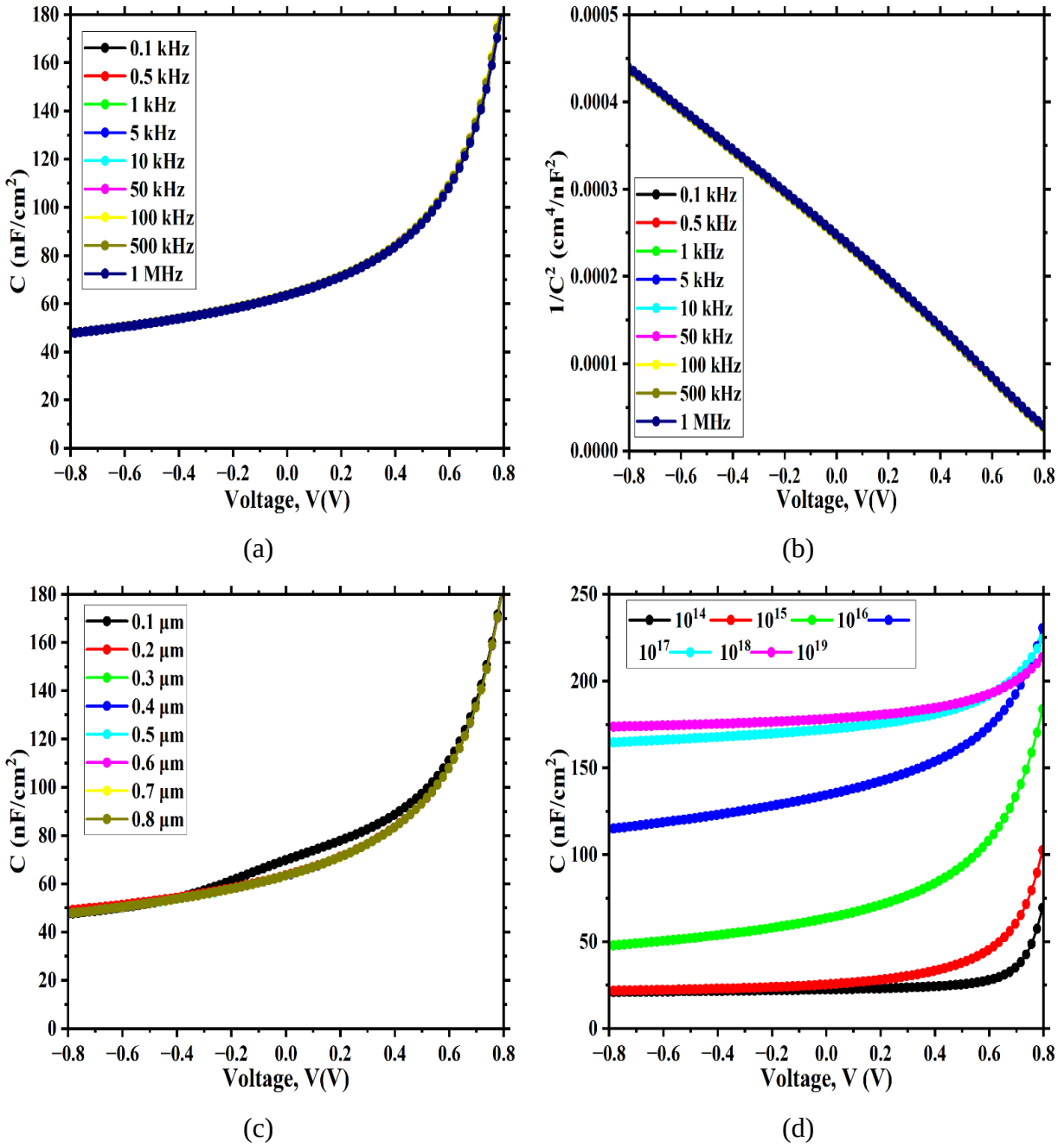

Fig: The impact of C-V parameters on SC (a) varying frequency (b) $1/C^2$ vs V curve (c) varying absorber thickness and (d) varying absorber doping concentration.

The depletion width (W_d) and the length of carrier diffusion can be calculated by these two obtained values (V_{bi}, V), by the following two relations [24]:

$$W_d = \left(\frac{2\varepsilon_s\varepsilon_0 V_{bi}}{qNa}\right)^{0.5} \ldots\ldots\ldots\ldots\ldots\ldots\ldots\ldots\ldots\ldots\ldots\ldots\ldots\ldots (7)$$

$$L_n \sim \sqrt{D_n\tau} = \sqrt{\mu_n \frac{kT}{q}\tau} \ldots\ldots\ldots\ldots\ldots\ldots\ldots\ldots\ldots\ldots\ldots\ldots\ldots\ldots (8)$$

Where D_n is the diffusivity of the electrons, τ is the minority career lifetime, μ_n is the electron mobility, $\frac{kT}{q}$ is the thermal voltage at room temperature. Before recombination, electrons may travel by this average distance towards the boundary of the space charge region. The active thickness required for the photocurrent in a $MoTe_2$ Solar structure can now be easily determined through the equation $L_p=L_n+W_d$ [24].

3.8. The final output performance $MoTe_2$ solar structure

There is two $MoTe_2$-based heterostructure solar cell. One is the baseline (without HTL) $MoTe_2$ SC structure and the other is the displayed (with HTL) heterojunction SC design of Al/FTO/CdS/$MoTe_2$/Sb_2S_3/Pt, where Sb_2S_3 has been used as an HTL layer and placed within left contact and $MoTe_2$ absorber layer. Figure 9(a) represents a comparison of the J-V curve of baseline and proposed SC structures. The thickness of FTO, Sb_2S_3, $MoTe_2$, CdS and has been chosen as 0.05 μm, 0.1 μm, 0.5 μm, 0.05 μm, respectively. It has been demonstrated that the PV performance of this displayed SC design is greater than the reference $MoTe_2$ solar structure. The PV parameters of the baseline $MoTe_2$ SC are 0.95 V, 38.15 mA/cm^2, 81.09%, and 29.35%, respectively. While the enhanced η of the presented Al/FTO/CdS/$MoTe_2$/Sb_2S_3/Pt SC is 40.33% containing V_{oc} of 1.13 V, J_{sc} of 40.78 mA/cm^2, and FF of 87.63%. The absorber layer with Sb_2S_3 HTL creates a strong electric field via the creation at the p^+-p junction which contributes to a degradation at the carrier recombination rate at the $MoTe_2$/Sb_2S_3 interface [21] [26] [27] [46] [47]. This reduction of carrier recombination contributes to enhancing the performance of our presented solar structure.

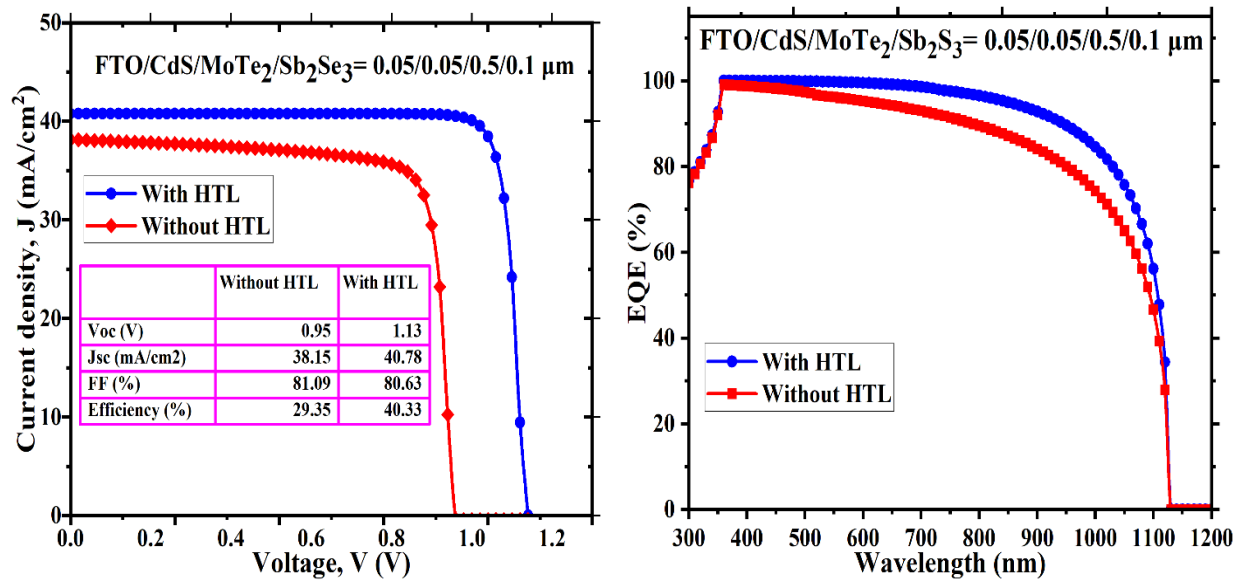

(a) **(b)**

Figure 9. (a) Simulated current density vs voltage (J-V) features and (b) EQE versus wavelength graph of the $MoTe_2$ SC in the presence and absence of HTL.

The wavelength-dependent external quantum efficiency (EQE) curves of $MoTe_2$ SC for both reference and presented structures have displayed in Fig. 9(b). It has also been cleared that the EQE of $MoTe_2$ SC with the HTL layer of solar cells is higher than without HTL and the wavelength has altered within (300~1200 nm) for detecting this effect. The enhancement of the EQE in the longer wavelength may be because of the insertion of the Sb_2S_3 HTL layer which diminishes carrier recombination by creating an electric field at the interface of $MoTe_2/Sb_2S_3$ [21] [40].

Table 4 reveals the comparison of the performance features of $MoTe_2$ SC studied by various research groups and proposed structures. This study shows that the η varied from 22.43% to 29.13% in the previously investigated $MoTe_2$ SC structures. The value of PV performance parameters is lower because of the mismatch of band arrangement at the Sb_2S_3/ $MoTe_2$ interface that inhibits the photo-generated carrier's conduction. Moreover, the presence of shallow and deep-level defects facilitates SRH recombination [47]. Thus the photovoltaic performances of $MoTe_2$ solar cell structure need to be enhanced. Our proposed structure has achieved better values by restricting carrier recombination at $Sb_2S_3/MoTe_2$ and $MoTe_2$/CdS layers [47]. The present study

of Al/FTO/CdS/$MoTe_2$/Sb_2S_3/Pt SC demonstrates insight into the development of high-efficiency $MoTe_2$ SC by suppressing carrier recombination.

Table 4: Comparison values of PV parameters with various research works.

No	Structure	Depth (μm)	V_{oc} (V)	Jsc (mA/cm^2)	FF (%)	PCE (%)	References
1	FTO/ZnO/$MoTe_2$/Cu_2Te	0.5	0.88	38.14	85.26	29.13	[1]
2	ZnO/Zn2SO4/CdS/CdTe/$MoTe_2$	0.08	0.7	28	---	28.00	[8]
3	CdS/$MoTe_2$/As_2Te_3	0.1-10	1.07	27.79	84.20	25.06	[10]
4	CdS/$MoTe_2$/In_2Te_3	0.1-5.0	1.07	27.90	84.20	25.17	[14]
5	FTO/CdS/CdTe/Sb_2S_3	1.0	1.15	28.74	86.03	28.41	[19]
6	SnO_2/Zn_2SnO_4/CdS/CdTe/ZnTe	0.1-2.9	1.05	24.34	87.20	22.43	[48]
7	SnO_2/Zn_2SnO_4/CdS/CdTe/SnTe	0.1-3.0	1.05	24.40	87.20	22.48	[49]
8	Zn_2SnO_4/CdS/$MoTe_2$/CZT	0.1-10	1.07	27.85	84.10	25.11	[13]
9	Al/FTO/CdS/$MoTe_2$/Pt (without HTL)	0.5	0.95	38.15	81.09	29.35	Proposed SC
10	Al/FTO/CdS/$MoTe_2$/Sb_2S_3/Pt (with HTL)	0.5	1.13	40.78	87.63	40.33	Proposed SC

4. Conclusions

In this study, we have constructed Al/FTO/CdS/$MoTe_2$/Sb_2S_3/Pt heterojunction PV solar structure with Sb_2S_3 HTL layer. Utilizing the SCAPS-1D simulator, the simulation successfully examined and compared the PV performances in the presence and absence of Sb_2S_3 HTL. We have extensively investigated the PV parameters due to the changes in thickness, doping density, temperature, series as well as shunt resistances. The impact of Sb_2S_3 HTL insertion has been explored in this research for $MoTe_2$-based PV cells to acquire the highest efficiency through lower absorber thickness. The constructed Al/FTO/CdS/$MoTe_2$/Sb_2S_3/Pt solar structure with Sb_2S_3 HTL has performed the η of 40.33%, FF of 87.63%, V_{oc} of 1.13 V, J_{sc} of 40.78 mA/cm^2 optimizing thickness of 0.5 μm of $MoTe_2$ absorber layer. While the baseline Al/FTO/CdS/$MoTe_2$/Pt solar cell has η of 29.35%, V_{oc} of 0.95 V, J_{sc} of 38.15 mA/cm^2, and FF of 81.09%. The presence of the Sb_2S_3 HTL generates an electric force at the P^+-P interface, leading to a decrease in carrier recombination. The decrease of carrier recombination contributes to enhancing the performance

parameters e.g. V_{oc}, J_{sc}, FF, and η. These findings indicate that $MoTe_2$-based heterojunction may be implemented in the solar semiconductor community in a cost-effective as well as feasible way.

Disclosures:

The authors confess here no competing financial or personal interests.

Acknowledgement:

The authors here are greatly recognized by Dr. Marc Burgelman and the entire of his team at the Department of Electronics and Information Systems (EIS), the University Of Gent, Belgium for allowing scope to use the SCAPS-1D software.

References

[1] Faisal, S. et al. (2017). Numerical analysis of MoTe2 thin film solar cell with Cu2Te BSF layer. *IEEE Region 10 Annual International Conference, Proceedings/TENCON*. DOI: 10.1109/TENCON.2017.8228252.

[2] Yoon, H. et al. (2011). Rim2, a pyrimidine nucleotide exchanger, is needed for iron utilization in mitochondria. *Biochemical Journal*. DOI: 10.1042/BJ20111036.

[3] Lee, T.D. and Ebong, A.U. (2017). A review of thin film solar cell technologies and challenges. *Renewable and Sustainable Energy Reviews*. DOI: 10.1016/j.rser.2016.12.028.

[4] Chopra, K.L. et al. (2004). Thin-film solar cells: An overview. *Progress in Photovoltaics: Research and Applications*. DOI: 10.1002/pip.541.

[5] Green, M.A. et al. (2018). Solar cell efficiency tables (version 52). *Progress in Photovoltaics: Research and Applications*. DOI: 10.1002/pip.3040.

[6] Beal, A.R. et al. (1972). Transmission spectra of some transition metal dichalcogenides. I. Group IVA: Octahedral coordination. *Journal of Physics C: Solid State Physics*. DOI: 10.1088/0022-3719/5/24/015.

[7] Böker, T. et al. (2001). Band structure of (formula presented) (formula presented) and (formula presented) Angle-resolved photoelectron spectroscopy and ab initio calculations. *Physical Review B - Condensed Matter and Materials Physics*. DOI: 10.1103/PhysRevB.64.235305.

[8] Moustafa, M. and AlZoubi, T. (2018). Effect of the n-MoTe2 interfacial layer in cadmium telluride solar cells using SCAPS. *Optik*. DOI: 10.1016/j.ijleo.2018.05.112.

[9] Wang, Z. et al. (2014). The structure and stability of molybdenum ditelluride thin films. *International Journal of Photoenergy*. DOI: 10.1155/2014/956083.

[10] Dey, M. et al. (2017). Design of highly stable and efficient molybdenum telluride PV cells with arsenic telluride BSF. *2016 3rd International Conference on Electrical Engineering and Information and Communication Technology, iCEEiCT 2016*. DOI: 10.1109/CEEICT.2016.7873153.

[11] Dey, M. et al. (2017). Enhancement the performance of molybdenum telluride solar cells with zinc telluride BSF. *2016 International Conference on Innovations in Science, Engineering and Technology, ICISET 2016*. DOI: 10.1109/ICISET.2016.7856534.

[12] Pan, S. et al. (2017). Ultrafast charge transfer between MoTe2 and MoS2 monolayers. *2D Materials*. DOI: 10.1088/2053-1583/4/1/015033.

[13] Dey, M. et al. (2017). Performance improvement of highly stable molybdenum telluride solar cells with CZT BSF. *ECCE 2017 - International Conference on Electrical, Computer and Communication Engineering*. DOI: 10.1109/ECACE.2017.7913038.

[14] Dey, M. et al. (2016). High performance and stable molybdenum telluride PV cells with Indium Telluride BSF. *ICDRET 2016 - 4th International Conference on the Developments in Renewable Energy Technology*. DOI: 10.1109/ICDRET.2016.7421495.

[15] Bansal, S. et al. (2019). Enhanced optoelectronic properties of bilayer graphene/HgCdTe-based single- A nd dual-junction photodetectors in long infrared regime. *IEEE Transactions on Nanotechnology*. DOI: 10.1109/TNANO.2019.2931814.

[16] Choi, Y.C. and Seok, S. Il (2015). Efficient Sb2S3-sensitized solar cells via single-step deposition of Sb2S3 using S/Sb-ratio-controlled SbCl3-thiourea complex solution. *Advanced Functional Materials*. DOI: 10.1002/adfm.201500296.

[17] Versavel, M.Y. and Haber, J.A. (2007). Structural and optical properties of amorphous and crystalline antimony sulfide thin-films. *Thin Solid Films*. DOI: 10.1016/j.tsf.2007.03.043.

[18] Rahman, S. et al. (2021). Photovoltaic performance enhancement in CdTe thin-film heterojunction solar cell with Sb 2 S 3 as hole transport layer. *Solar Energy*. DOI: 10.1016/j.solener.2021.10.036.

[19] Haque, M.D. et al. (2021). Efficiency enhancement of WSe2 heterojunction solar cell with CuSCN as a hole transport layer: A numerical simulation approach. *Solar Energy*. DOI: 10.1016/j.solener.2021.10.054.

[20] Cao, Y. et al. (2019). Towards high efficiency inverted Sb2Se3 thin film solar cells. *Solar Energy Materials and Solar Cells*. DOI: 10.1016/j.solmat.2019.109945.

[21] Casas, G.A. et al. (2017). Analysis of the power conversion efficiency of perovskite solar cells with different materials as Hole-Transport Layer by numerical simulations. *Superlattices and Microstructures*. DOI: 10.1016/j.spmi.2017.04.007.

[22] Ahmed, S.R. Al et al. (2021). Performance enhancement of Sb2Se3 solar cell using a back surface field layer: A numerical simulation approach. *Solar Energy Materials and Solar Cells*. DOI: 10.1016/j.solmat.2020.110919.

[23] Basak, A. and Singh, U.P. (2021). Numerical modelling and analysis of earth abundant Sb2S3 and Sb2Se3 based solar cells using SCAPS-1D. *Solar Energy Materials and Solar Cells*. DOI: 10.1016/j.solmat.2021.111184.

[24] Burgelman, M. et al. (2000). Modelling polycrystalline semiconductor solar cells. *Thin Solid Films*. DOI: 10.1016/S0040-6090(99)00825-1.

[25] Atowar Rahman, M. (2021). Enhancing the photovoltaic performance of Cd-free Cu2ZnSnS4 heterojunction solar cells using SnS HTL and TiO2 ETL. *Solar Energy*. DOI: 10.1016/j.solener.2020.12.020.

[26 Rahman, M.A. (2021). Design and simulation of a high-performance Cd-free Cu2SnSe3 solar cells with SnS electron-blocking hole transport layer and TiO2 electron transport layer by SCAPS-1D. *SN Applied Sciences*. DOI: 10.1007/s42452-021-04267-3.

[27] Hosen, A. et al. (2021). Simulating the performance of a highly efficient CuBi2O4-based thin-film solar cell. *SN Applied Sciences*. DOI: 10.1007/s42452-021-04554-z.

[28] Tao, J. et al. (2019). Investigation of electronic transport mechanisms in Sb 2 Se 3 thin-film solar cells. *Solar Energy Materials and Solar Cells*. DOI: 10.1016/j.solmat.2019.04.003.

[29] Xiao, Y. et al. (2020). Numerical simulation and performance optimization of Sb2S3 solar cell with a hole transport layer. *Optical Materials*. DOI: 10.1016/j.optmat.2020.110414.

[30] Amin, N. et al. (2007). Numerical modeling of CdS/CdTe and CdS/CdTe/ZnTe solar cells as a function of CdTe thickness. *Solar Energy Materials and Solar Cells*. DOI: 10.1016/j.solmat.2007.04.006.

[31] Chen, C. et al. (2018). Efficiency Improvement of Sb2Se3 Solar Cells via Grain Boundary Inversion. *ACS Energy Letters*. DOI: 10.1021/acsenergylett.8b01456.

[32] Khatun, M.M. et al. (2021). Numerical investigation on performance improvement of WS2 thin-film solar cell with copper iodide as hole transport layer. *Solar Energy*. DOI: 10.1016/j.solener.2021.06.062.

[33] Singh, P. and Ravindra, N.M. (2012). Temperature dependence of solar cell performance - An analysis. *Solar Energy Materials and Solar Cells*. DOI: 10.1016/j.solmat.2012.02.019.

[34] Laidouci, A. et al. (2020). Numerical study of solar cells based on ZnSnN2 structure. *Solar Energy*. DOI: 10.1016/j.solener.2020.09.025.

[35] Varshni, P. (1967). Temperature dependence of the energy gap in semiconductors.

[36] Da, Y. and Xuan, Y. (2013). Role of surface recombination in affecting the efficiency of nanostructured thin-film solar cells. *Optics Express*. DOI: 10.1364/oe.21.0a1065.

[37] Mohammad, H. and Science, D. Optical Materials Numerical Analysis for the Efficiency Enhancement of MoS2 Solar Cell : A Simulation Approach by SCAP-1D Department of Electronics and Communication Engineering , Hajee Mohammad Danesh Science.

[38] Wang, Y. et al. (2015). Towards printed perovskite solar cells with cuprous oxide hole transporting layers: A theoretical design. *Semiconductor Science and Technology*. DOI: 10.1088/0268-1242/30/5/054004.

[39] Xiao, D. and Balcom, B.J. (2017). BLIPPED (BLIpped Pure Phase EncoDing) high resolution MRI with low amplitude gradients. *Journal of Magnetic Resonance*. DOI: 10.1016/j.jmr.2017.10.013.

[40] Ali, M.H. et al. (2023). Performance Enhancement of an MoS2-Based Heterojunction Solar Cell with an In2Te3 Back Surface Field: A Numerical Simulation Approach. *ACS Omega*. DOI: 10.1021/acsomega.2c07846.

[41] Hennel, A.M. (1971). Temperature dependence of the energy gap in GaAs. *Physica Status Solidi (a)*. DOI: 10.1002/pssa.2210080244.

[42] Islam, S. et al. (2021). Defect Study and Modelling of SnX3-Based Perovskite Solar Cells with SCAPS-1D.

[43] Amiri, M. et al. (2020). Performance enhancement of ultrathin graded Cu(InGa)Se2 solar cells through modification of the basic structure and adding antireflective layers. *Journal of Photonics for Energy*. DOI: 10.1117/1.jpe.10.024504.

[44] Pal, D. and Das, S. (2021). C-V and I-V Characterisation of CdS/CdTe Thin Film Solar Cell Using Defect Density Model. *Serbian Journal of Electrical Engineering*. DOI: 10.2298/SJEE2102255P.

[45] Zahoo, R.K. and Saleh, A.N. (2021). Effect Of Carrier Concentration And Thickness Of Absorber Layer On Performance CBTS Solar Cell. *Turkish Journal of Computer and Mathematics Education*.

[46] Dey, M. et al. (2015). Design of high efficient and stable ultra-thin CdTe solar cells with ZnTe as a potential BSF. *2015 International Conference on Green Energy and Technology, ICGET 2015*. DOI: 10.1109/ICGET.2015.7315079.

[47] Dey, M. et al. (2016). Design of high performance and ultra-thin CdTe solar cells with SnTe BSF from numerical analysis. *2015 18th International Conference on Computer and Information Technology, ICCIT 2015*. DOI: 10.1109/ICCITechn.2015.7488136.